Doubled-Frequency Triangular Current Mode Modulation With Sinusoidal Frequency Profile for a Three-Level ANPC Converter

Gang Zhang, *Student Member, IEEE*, Yang Wu, *Student Member, IEEE*, Rui Qiang, *Student Member, IEEE*, Prasanth Venugopal, *Senior Member, IEEE*, Junzhong Xu, *Member, IEEE*, and Thiago Batista Soeiro, *Senior Member, IEEE*

***Abstract*—Triangular current mode (TCM) modulation is a well-researched technique for optimizing the trade-off between converter power or gravimetric density and power efficiency. However, its application in multilevel ac–dc converters has been limited. This article extends the TCM concept to a three-level active-neutral-point-clamped converter and addresses key implementation challenges. First, two fundamental TCM commutation sequences are introduced. Building on these, a doubled-frequency TCM (DF-TCM) modulation method is proposed to offer additional benefits. A major drawback of conventional TCM is its complex switching frequency profile, which imposes significant computational burdens and can easily excite circuit resonance. To address this, this article proposes replacing it with sinusoidal frequency profiles. In addition, considerations for parameter design are discussed, and a model for semiconductor conduction losses is developed. Finally, a hardware prototype is constructed to validate the feasibility of the proposed DF-TCM strategy.**

***Index Terms*—Active neutral-Point-clamped (ANPC) converter, multilevel converter, power factor correction (PFC), triangular current mode (TCM), zero voltage switching (ZVS).**

I. Introduction

MULTILEVEL converters are extensively used in medium to high power applications, including motor drives, high-voltage photovoltaic (PV) systems, wind energy generation, and electric vehicles (EVs). Their advantages include lower harmonic distortion, high power efficiency at medium to high switching frequencies, reduced $\mathrm{d}v/\mathrm{d}t$, and an increased effective switching frequency [1], [2], [3], [4], [5]. Among the various multilevel topologies, the three-level neutral-point-clamped (3L-NPC) converter, shown in Fig. 1(a), is one of the most widely studied and implemented. Originally patented by Baker [6] and later introduced in an academic paper by Nabae [7], the 3L-NPC topology offers a relatively simple circuit structure while effectively reducing the voltage blocking requirement of its semiconductor devices to approximately half of the dc-link voltage.

A variation of the 3L-NPC, known as the three-level active neutral-point-clamped (3L-ANPC) converter, is shown

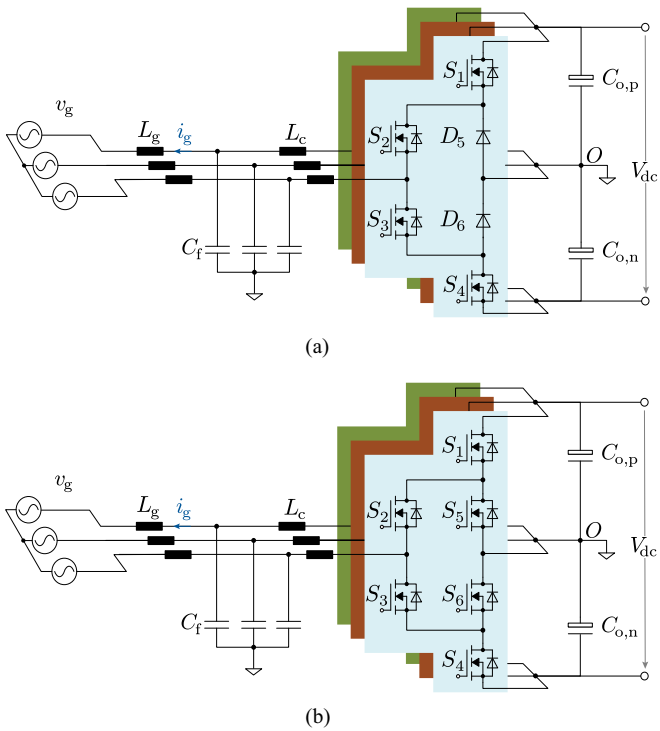

Fig. 1. Circuit diagrams of (a) a 3L-NPC converter; (b) a 3L-ANPC converter.

Received 24 February 2025; revised 27 May 2025; accepted 27 June 2025. Date of publication 30 June 2025; date of current version 5 August 2025. Recommended for publication by Associate Editor A. Safaee. *(Corresponding author: Gang Zhang.)*

Gang Zhang, Rui Qiang, Prasanth Venugopal, and Thiago Batista Soeiro are with the Power Electronics and Electromagnetic Compatibility Group, University of Twente, 7522 NH Enschede, The Netherlands (e-mail: g.zhang-1@utwente.nl; r.qiang@utwente.nl; prasanth.venugopal@utwente.nl; t.batistasoeiro@utwente.nl).

Yang Wu is with ABB Corporate Research Sweden, 722 26 Vasteras, Sweden (e-mail: yang.wu@se.abb.com).

Junzhong Xu is with the School of Electrical Engineering, Shanghai Jiao Tong University, Shanghai 200240, China, and also with the Key Laboratory of Control of Power Transmission and Conversion, Ministry of Education, Shanghai 200240, China (e-mail: junzhongxu@sjtu.edu.cn).

Color versions of one or more figures in this article are available at https://doi.org/10.1109/TPEL.2025.3584858.

Digital Object Identifier 10.1109/TPEL.2025.3584858

in Fig. 1(b). This topology was introduced and patented by ABB [8]. The 3L-ANPC circuit is derived from the 3L-NPC topology by replacing the two discrete clamping diodes with active power switches such as MOSFETs or IGBTs with antiparallel diodes [9], [10]. This modification enables power loss balancing, enhances thermal management, extends the converter's lifespan, increases the maximum switching frequency, and improves output power capability by ensuring more uniform utilization of all power devices [9], [11].

From a power conversion efficiency standpoint, the 3L-ANPC converter does not provide a substantial reduction in total power losses compared to the 3L-NPC topology. The key differences lie in conduction and switching losses. Replacing the bipolar clamping diodes with unipolar MOSFETs impacts conduction losses, while switching losses are influenced by reverse recovery characteristics. Specifically, the 3L-NPC topology experiences dynamic losses due to the discrete diode, whereas the 3L-ANPC configuration is affected by the MOSFET's body-diode switching losses.

In a MOSFET-based 3L-ANPC circuit, losses generated in the power devices mainly consist of conduction losses due to the ON-resistance $R_{\mathrm{ds,on}}$ and switching losses that are generated at each instant of circuit commutation. When the converter system is working at high switching frequencies in an effort to improve the power density of passive filters, switching losses become more prominent. Especially for the state-of-the-art wide-bandgap (WBG) devices such as SiC MOSFETs that offers relatively low $R_{\mathrm{ds,on}}$, switching losses can account for over 70% of the total semiconductor losses, of which the turn-ON losses are usually greater than the turn-OFFones [12], [13]. To increase the system efficiency while maintaining a relatively high switching frequency, it is crucial to implement a soft switching technique, for example, zero voltage switching (ZVS), which can significantly decrease the switching losses.

Triangular current mode (TCM) modulation is a well-studied soft-switching technique that enables ZVS turn-ON for power switches by leveraging existing magnetic components and parasitic capacitance, eliminating the need for additional auxiliary circuits. During commutation, the inductor current reverses polarity, allowing the parasitic output capacitor of the switch to discharge to zero before its body-diode conducts, ensuring ZVS activation when the gate signal is applied [12]. The inductor current follows a triangular waveform, toggling polarity twice per switching cycle (hence the name TCM). This technique has been widely adopted across various ac–dc and dc–dc converter topologies, including three-phase two-level voltage source inverters, single-phase full-bridge rectifiers, and four-switch buck–boost converters [14], [15], [16], [17], [18], [19]. Note that, as discussed in [14], for the three-phase three-wire ac–dc implementation of TCM, a virtual ground (VG) path for the zero-sequence components of the ac current is necessary to shape the triangular waveform. An example of VG connection enabling the TCM operation of the 3L-NPC and 3L-ANPC converters are shown in Fig. 1(a) and (b), respectively.

While TCM has been widely applied across different converter topologies, its use in multilevel ac–dc converters remains relatively underexplored. In [20], the electromagnetic interference (EMI) performance of a three-level T-type (3 L T-type) inverter using TCM is analyzed in detail. Unlike the 3 L T-type, which requires the upper and lower switches to block the full dc-link voltage, the 3L-ANPC topology ideally has voltage stress of half the dc-link across all six switches. This article builds on that foundation by exploring TCM implementation in the 3L-ANPC, which offers more modulation flexibility than the 3 L T-type and shows promising potential for power loss distribution among the power devices. Specifically, two alternative TCM methods tailored for the 3L-ANPC converter are developed, incorporating a combination of high-frequency (HF) and low-frequency (LF) switching modules. By integrating these two approaches, a doubled-frequency TCM (DF-TCM) modulation strategy is naturally formulated, offering additional advantages. Conventional TCM modulation, however, involves a time-varying switching frequency profile, which imposes a heavy computational burden on microcontrollers, complicates theoretical analysis, and increases susceptibility to circuit resonance. To mitigate these challenges, this article proposes replacing the conventional approach with a sinusoidal frequency profile (SFP). This alternative maintains nearly the same ZVS turn-ON capability throughout the utility cycle while significantly simplifying computational requirements.

A key challenge of TCM modulation is its inherently large current ripple, which can violate grid harmonic regulations and necessitate larger supra-harmonic and EMI filters. Two primary approaches exist to mitigate this issue: integrated TCM (iTCM) [15], [21]; and interleaved TCM [18], [22]. The iTCM topology incorporates a branch notch filter that confines a portion of the HF current ripple within the branch circuit and phase-leg, preventing it from propagating to the ac side (grid or machine side). Conversely, the interleaved TCM topology reduces grid or machine-side current ripple by parallelizing multiple switching cells and operating them in an symmetrically interleaved manner. This article addresses these concerns and provides both theoretical and experimental validation on how iTCM and interleaved TCM can be implemented in the studied circuit alongside the fundamental TCM strategy.

All in all, this article contributes to the following:

1) The TCM modulation strategy is extended to the 3L-ANPC converter, with an in-depth discussion on practical implementation challenges.
2) Two fundamental TCM modulation methods are proposed for the studied circuit, forming the basis for the development of a more advantageous DF-TCM modulation strategy.
3) The concept of SFP is proposed as a practical solution to overcome the drawbacks of conventional frequency profiles.

The rest of this article is organized as follows. Section II provides a brief overview of the 3L-ANPC converter's operation and details the working principles of TCM modulation specific to this topology, followed by the derivation of the DF-TCM strategy. A practical implementation approach incorporating SFP is then introduced. Section III discusses the system parameters used in hardware experiments and presents analytical models for

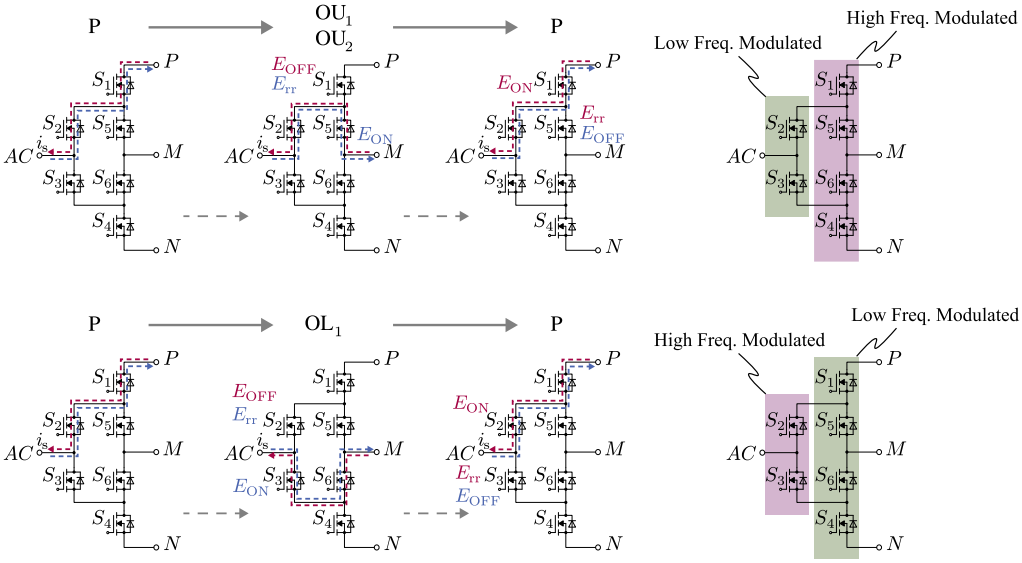

Fig. 2. Switching loss generated for the corresponding current commutation sequences.

TABLE I
SWITCHING STATES OF A THREE-LEVEL ANPC CONVERTER

State	Terminal Volt.	S_1	S_2	S_3	S_4	S_5	S_6
P	$V_{dc}/2$	1	1	0	0	0	1
N	$-V_{dc}/2$	0	0	1	1	1	0
OU_1	0	0	1	0	1	1	0
OU_2	0	0	1	0	0	1	0
OL_1	0	1	0	1	0	0	1
OL_2	0	0	0	1	0	0	1

conduction losses. Section IV validates the functionality of the proposed converter system using a hardware prototype. Finally, Section V concludes this article.

II. CIRCUIT TOPOLOGY AND MODULATION METHOD

A. Operation of 3L-ANPC Converter

The circuit topology of a 3L-ANPC converter is illustrated in Fig. 1(b), where S_1 and S_4 are the outer switches, S_2 and S_3 are the inner switches, and S_5 and S_6 function as the clamping switches. The switching states and the corresponding voltages at the switching node of the phase terminal are summarized in Table I. A key distinction between the 3L-ANPC and the conventional 3L-NPC topology is that the 3L-ANPC converter features four redundant zero states (i.e., OU_1, OU_2, OL_1, and OL_2), whereas the 3L-NPC or 3L T-type topologies have only one [7]. This additional degree of freedom allows for precise control of switching losses during commutation and current flow during the implementation of the zero state. Notably, S_6 should be turned ON during the "P" state to ensure that S_3 and S_4 equally share the dc-link voltage when in OFF-state. Similarly, S_5 should be turned on during the "N" state for the same reason. Among the four redundant zero states, "OU_1" and "OU_2" involve the upper inner switch S_2 and upper clamping switch S_5 conducting the freewheeling current, while "OL_1" and "OL_2" involve the lower inner switch S_3 and lower clamping switch S_6. The only distinction between "OU_1" and "OU_2" (or between "OL_1" and "OL_2") is the switching state of S_4 (or S_1), which does not impact the free-wheeling path. The selection of the appropriate zero states depends on the next switching transition. If S_4 (or S_1) is required to be on in the upcoming switching state, preturning it on enables zero-current switching (ZCS). In such cases, "OU_2" (or "OL_2") should be chosen to facilitate this transition efficiently.

B. Working Principles of TCM on 3L-ANPC Converter

One of the primary causes of switching losses during commutation is the overlap between current and voltage waveforms. Considering the switching commutations of the phase-leg of a 3L-ANPC circuit in Fig. 2, when the switched phase current i_s is positive and alternates between the "P" state and the "OU" state, as shown in Fig. 2, turn-OFFloss E_{OFF} occurs in S_1 during the transition from "P" to "OU," while turn-ON loss E_{ON} and reverse recovery loss E_{rr} occurs in S_1 and S_5, respectively, during the transition from "OU" to "P." Conversely, if i_s flows in the reverse direction, E_{ON} and E_{OFF} occurs in S_5, while E_{rr} appears in S_1, following the exact opposite pattern. For MOSFETs, particularly those based on WBG technology, E_{ON} is typically much greater than E_{OFF} and E_{rr}. Notably, E_{ON} occurs only when transitioning from "OU" to "P" for positive i_s and from "P" to "OU" for negative i_s. However, in TCM, i_s is modulated such that it remains positive during the transition from "P" to "OU" and negative during the transition from "OU" to "P." This ensures that E_{ON} is mitigated, thereby achieving ZVS turn-ON. A similar loss analysis applies to the commutation between the "P" state and the "OL_1" state in Fig. 2.

ZVS turn-ON avoids E_{ON} losses by utilizing i_s to discharge the parasitic output capacitor of the switch, $C_{oss,Q}$, to zero before the switch is commanded to turn ON. This requires i_s to flow in

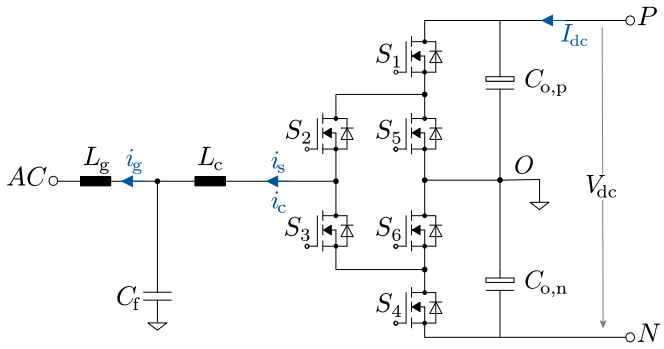

Fig. 3. Circuit diagram for a single phase of a TCM-modulated 3L-ANPC converter with LCL filter on AC side.

the direction of the body-diode of the switch being turned ON at the switching instant. Once i_s has fully discharged $C_{oss,Q}$, it freewheels through the body-diode until the turn-ON gate signal is applied. Since the gate signal is only applied after the voltage across the switch drops to zero, the transition remains soft. The soft-switching process is essentially a resonance between the effective ac-side inductance L_c and the equivalent capacitance C_{eq}, which can be represented by the u-Zi diagram as discussed in [12]. Usually, L_c is much larger than C_{eq}, and therefore, during resonance i_s can be viewed as constant. Based on this assumption, the minimum current required for full ZVS turn-ON I_{zvs} can be derived as (1) in terms of Q_{oss}, the charge stored in C_{eq}, or equivalently as (2) in terms of the charge-equivalent capacitance $C_{eq,Q}$ [23]. $C_{eq,Q}$ is dominated by the switching devices $C_{oss,Q}$, PCB added drain-to-source parasitic capacitance $C_{pcb,Q}$, and L_c winding capacitance $C_{wdg,Q}$, as given by (3)

$$|I_{zvs}| = \sqrt{2Q_{oss}\left(V_{dc}\right) \cdot V_{dc}/L_c} \tag{1}$$

$$|I_{zvs}| = \sqrt{2C_{eq,Q}\left(V_{dc}\right) \cdot V_{dc}^2/L_c} \tag{2}$$

$$C_{Q,eq} = 2C_{oss,Q} + 2C_{pcb,Q} + C_{wdg,Q}. \tag{3}$$

For a 3L-ANPC converter with an LCL filter, as depicted in Fig. 3, two fundamental TCM modulation schemes can be formulated, as summarized in Fig. 4. TCM-I operates by switching one outer switch and one clamping switch at the utility frequency (50 or 60 Hz), while the two inner switches are modulated at HF. Under this modulation strategy, the six switches in the phase leg are categorized into two LF-modulated modules and one HF-modulated module. During the positive half-cycle of the ac voltage (v_{ac}), switches S_1 and S_6 remain clamped, while S_2 and S_3 switch at HF to generate a PWM-modulated voltage that alternates between $+V_{dc}/2$ and 0 at the switching node. The circuit transitions between "P" and "OL$_2$." Similarly, during the negative half-cycle, switches S_4 and S_5 are clamped, while S_2 and S_3 are switched at HF, producing a PWM-modulated voltage that transitions between $-V_{dc}/2$ and 0 at the switching node. In this case, the switching states shift between the "N" state and "OU$_2$." To achieve ZVS transition, i_s must be positive during the commutation from S_2 to S_3 and negative during the transition from S_3 to S_2. Furthermore, i_s should be regulated such that its fundamental component matches the desired ac current magnitude $\hat{i}_{ac}$ given by (4), here P denotes the nominal power for a single-phase system

$$\hat{i}_{ac} = 2P/\hat{v}_{ac}. \tag{4}$$

The minimum required current ripples $\triangle i_s$ are then given by (5), where the phase θ is given by $\theta = \omega_0 t + \varphi_0$

$$\triangle i_s(\theta) = 2|I_{zvs}| + 2\hat{i}_{ac}|\sin(\theta)|. \tag{5}$$

The time allocations for the "P" state (t_p), and the "O" state (t_0), when $u_s > 0$, are given by (6), where L denotes the effective system inductance, which should approximate L_c. The time allocations for the "N" state and the "O" state when $u_s < 0$ can be derived in similar way

$$\begin{cases} t_p(\theta) = \frac{\triangle i_s(\theta)}{\frac{1}{2}V_{dc} - v_{ac}(\theta)} \cdot L \\ t_0(\theta) = \frac{\triangle i_s(\theta)}{v_{ac}(\theta)} \cdot L. \end{cases} \tag{6}$$

Based on the assumption that the converter works in the power factor correction (PFC) mode, the time function of the switching frequency f_{sw} can be then obtained as follows:

$$f_{sw}(\theta) = \frac{\hat{v}_{ac}^2 \cdot (\sin\theta - M \cdot \sin^2\theta)}{2\hat{v}_{ac} \cdot |I_{zvs}| + 4P \cdot \sin\theta} \cdot \frac{1}{L}. \tag{7}$$

Note that to maintain a constant reverse current $|I_{zvs}|$, TCM requires a time-varying switching frequency, as illustrated in Fig. 5. The switching frequency profile follows a periodic pattern with a period of 180°, and within each period, it exhibits symmetry about its centerline at 90°. Note that only under PFC operation, that is, when the power factor is unity, the switching frequency profile is symmetrical about 90°, which is an important feature for the analysis afterward. Therefore, for the rest of the article, only PFC operation is considered.

TCM-II, similar to TCM-I, employs a combination of HF and LF modulated modules. Under TCM-II, S_2 remains clamped, while S_1 and S_5 switch at HF during the positive half-cycle, causing the circuit to transition between the "P" state and "OU$_1$." During the negative half-cycle, S_3 is clamped, while S_4 and S_6 are switched at HF. This modulation scheme is summarized in Fig. 4(b). The current ripple constraints and the switching frequency profile for TCM-II are identical to those of TCM-I.

A well-known drawback of TCM modulation is the large current ripple required to achieve ZVS turn-ON, as defined by (5). In most applications, such large ripples cannot be directly injected into the ac side, necessitating measures to mitigate their impact. Currently, two widely adopted solutions address this issue: interleaved TCM and iTCM.

Fig. 6(a) illustrates the circuit diagram of an interleaved TCM-modulated 3L-ANPC converter. The interleaved TCM topology consists of multiple parallel-connected cells, each comprising a HF module and a converter-side filter inductor L_c. To ensure ZVS transitions for each pair of HF-modulated switches (S_2 and S_3) the minimum TCM current ripple, as defined in (4) and (5), must flow through each cell. In this case, the power P in (7) should be adjusted to reflect a fraction Nth of the total system

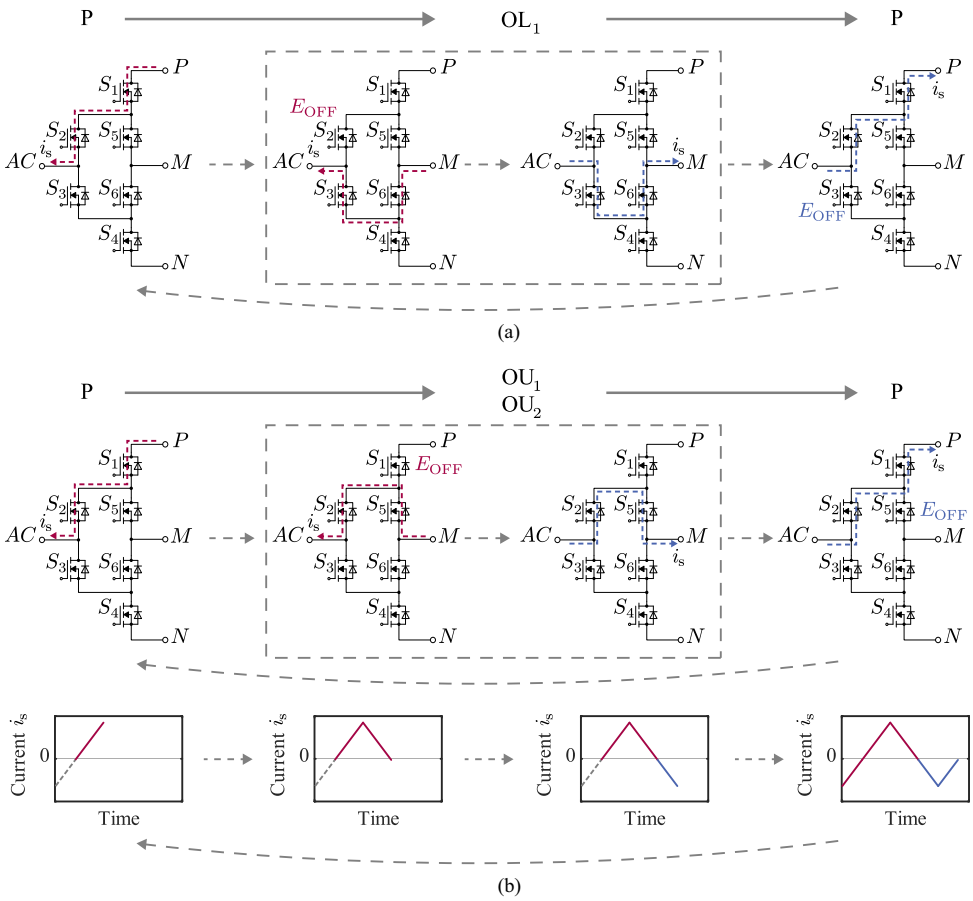

Fig. 4. Commutation sequences and correspondingly generated switching loss for: (a) TCM-I; (b) TCM-II.

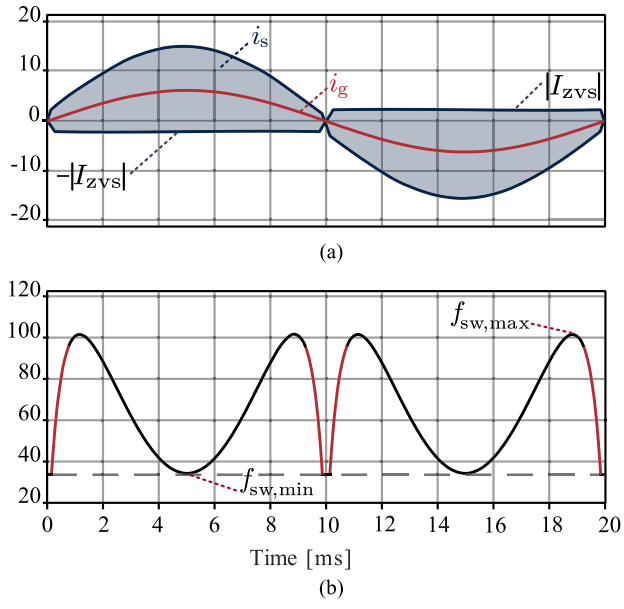

Fig. 5. Illustration of the waveforms of TCM modulation for the studied topology in one fundamental period: (a) The current flowing out of the switching node i_s and filtered current flowing into AC terminal i_g; (b) The instantaneous switching frequency function f_{sw}. (a) Current i_s and i_g [A]. (b) Switching Frequency [kHz].

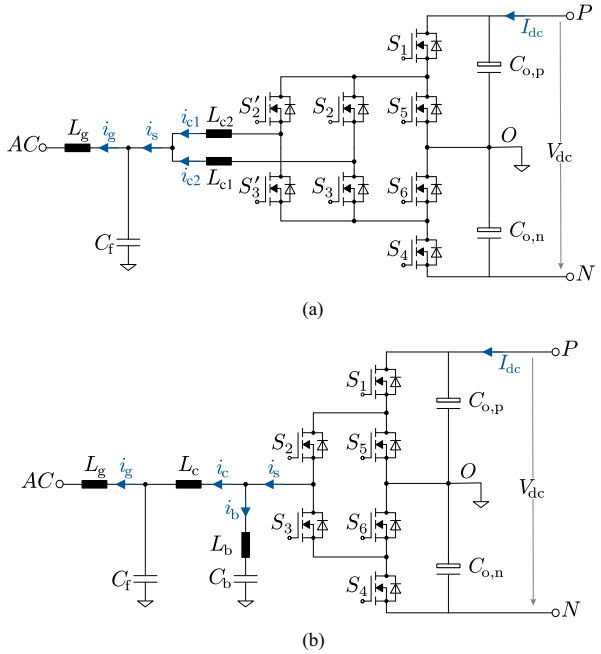

Fig. 6. Circuit diagrams for a single phase of (a) a 3L-ANPC converter with interleaved-TCM modulation; (b) a 3L-ANPC converter with iTCM modulation.

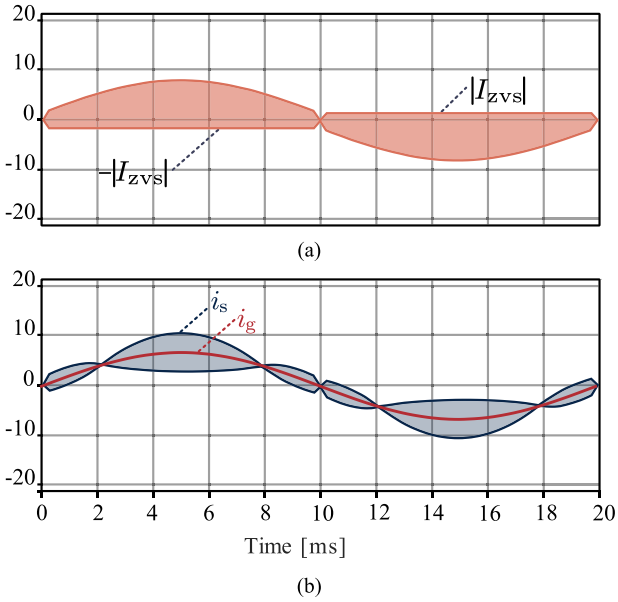

Fig. 7. Illustration of the waveform of the interleaved TCM waveforms for the studied topology in one fundamental period. (a) The inductor current i_{c1} and i_{c2}. (b) The current flowing out of the switching node i_s and the filtered current flowing into AC terminal i_g. (a) Current i_{c1} and i_{c2} [A]. (b) Current i_s and i_g [A].

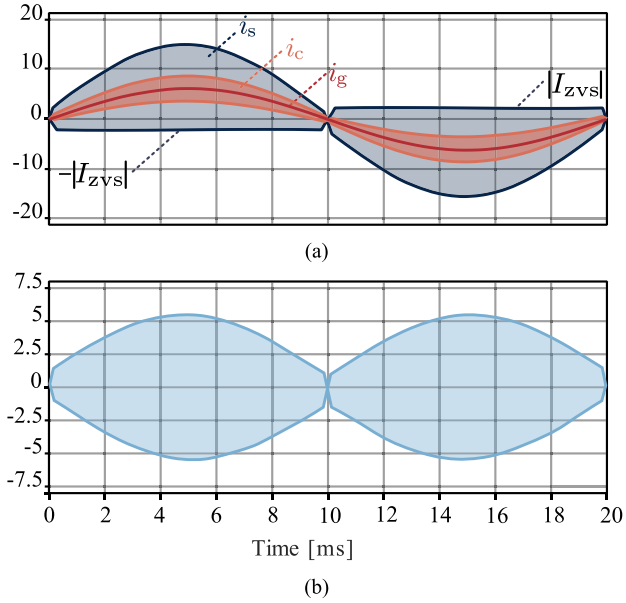

Fig. 8. Illustration of the waveform of the iTCM waveforms for the studied topology in one fundamental period. (a) The current flowing out of the switching node i_s, the inductor current i_c and the filtered current flowing into AC terminal i_g. (b) The current flowing into the notch filter i_b. (a) Current i_s, i_c and i_g [A]. (b) Filter Current i_b [A].

power, where N represents the number of parallel-connected cells. This circuit arrangement effectively mitigates output current ripple by operating the parallel cells in an symmetric interleaved manner. Specifically, the same modulation signal is applied to all cells, but their carrier signals are phase-shifted by $360^\circ/N$. For instance, in a two-cell configuration, as shown in Fig. 6(a), the two carrier signals are phase-shifted by 180°. Fig. 7 illustrates the main waveforms of interleaved TCM modulation with two parallel switching cells. It can be observed that the current triangular component or the current ripple in i_s, seen in Fig. 5, is distributed between i_{c1} and i_{c2}, where the current ripple are 180° out of phase. As a result, their sum, i_s, exhibits significantly reduced ripple, demonstrating the effectiveness of interleaving in minimizing current ripple. Notably, from the L_g and C_f design perspective, the two cells parallel interleaved 3L-ANPC topology depicted in Fig. 6(a) will function as an equivalent five-level ANPC (5L-ANPC) circuit.

Further details on the interleaved TCM method can be found in [12]. It is important to note that only TCM-I can be applied to this configuration. In contrast to the interleaved arrangement, both TCM-I and TCM-II can be implemented in the iTCM topology, as depicted in Fig. 6(b). In this topology, L_b and C_b form an integrated notch filter that effectively traps a portion of the TCM current ripple within the circuit. The proportion of ripple that remains and flows into the ac side is determined by the relationship between L_c and L_b. This current-division ratio, denoted as r, is expressed by (8). For a more detailed discussion on the iTCM method, refer to [15]

$$r = \frac{L_b}{L_c + L_b}. \tag{8}$$

Fig. 8 illustrates the operating waveforms of an iTCM-modulated ANPC converter. It can be observed that a significant portion of the current ripple is confined within the dc side by the notch filter as i_b, while only a small fraction remains in i_c, reducing the filtering requirements on the ac side.

C. DF-TCM Modulation

It can be observed from Fig. 4 that the roles of the HF and LF modulated modules are complementary in TCM-I and TCM-II. Specifically, the HF modules in TCM-I serve as the LF modules in TCM-II, and vice versa. DF-TCM, summarized in Fig. 9, can be regarded as a combination of TCM-I and TCM-II, where the two modulation methods alternate. As a result, all six switches operate at HF, but at half the frequency of the switched voltage at the switching node. From an implementation perspective, DF-TCM can be considered the TCM counterpart of DF-PWM, a PWM modulation strategy introduced in [24] for the 3L-ANPC topology. Assuming identical designs for the magnetic components and the same TCM current ripple, the HF modules in TCM-I and TCM-II switch at f_{sw}, whereas in DF-TCM, all switches operate at $f_{sw}/2$. Consequently, the switching frequency profile for DF-TCM is defined by the following:

$$f_{sw}(\theta) = \frac{1}{2} \cdot \frac{\hat{v}_{ac}^2 \cdot (\sin\theta - M \cdot \sin^2\theta)}{2\hat{v}_{ac} \cdot |I_{zvs}| + 4P \cdot \sin\theta} \cdot \frac{1}{L}. \tag{9}$$

Note that $f_{sw}(\theta)$ in (9) represents the actual switching frequency of each switch or the carrier frequency if a carrier-based PWM (CBPWM) method is used. However, the apparent switching frequency observed at the switching node remains defined by (7). As previously discussed, TCM-II is not compatible with the interleaved topology, meaning that DF-TCM can only be

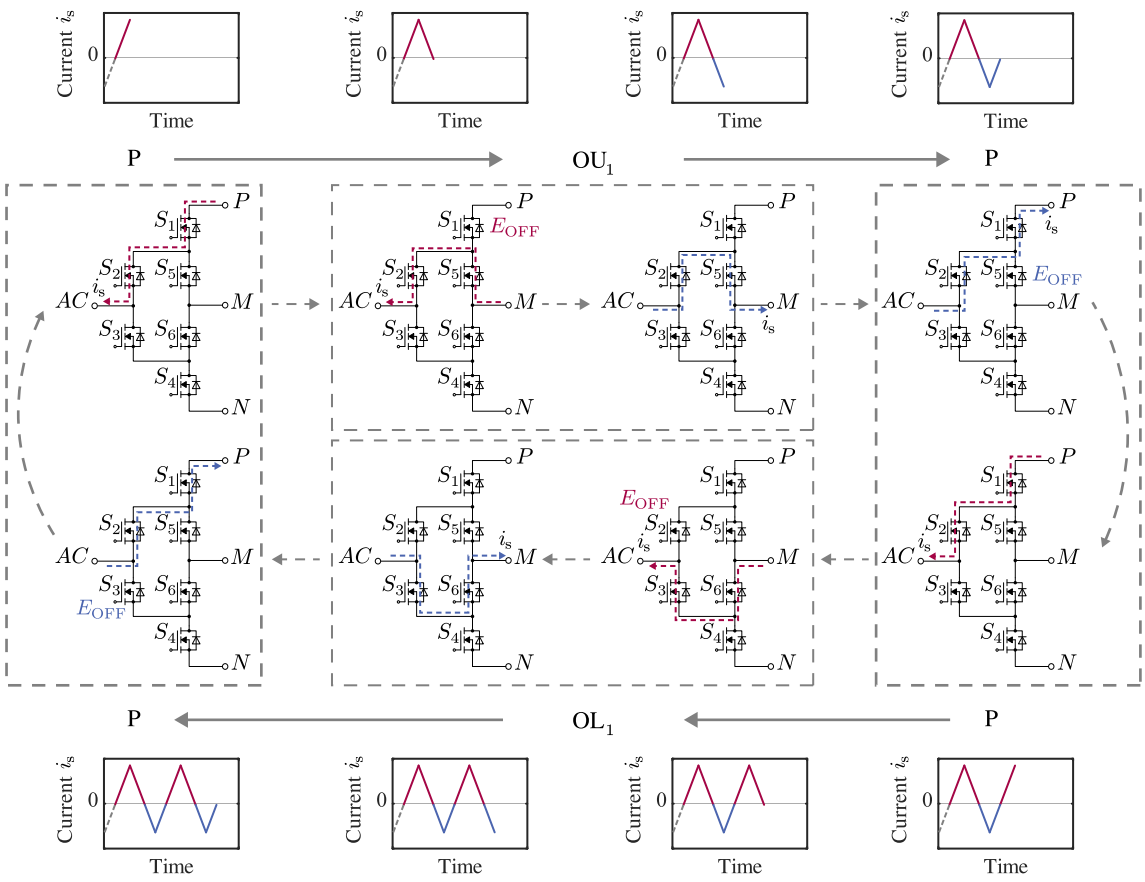

Fig. 9. Commutation sequences and correspondingly generated switching loss for DF-TCM.

implemented with the iTCM topology. Similar to its PWM counterpart, DF-TCM offers several advantages over TCM-I and TCM-II, including: maximizing the effective switching frequency achievable within the studied topology; greater immunity to dead-time effects, and; more balanced distribution of switching losses across all switches [24].

Although TCM strategy is capable of mitigating the turn-ON losses E_{ON}, which occur due to the overlap between rising current and falling voltage, significant losses still persist in each switching cycle, primarily due to turn-OFFtransitions and dielectric losses in the parasitic output capacitor. In other words, while TCM ensures soft turn-ON, it may still result in hard turn-OFFlosses [25], collectively referred to as residual ZVS losses in [26]. As a result, in conventional TCM schemes, HF-modulated switches experience higher losses due to their more frequent commutations compared to LF-modulated switches. This imbalance leads to thermal stress variations across different components, necessitating more complex thermal management. In contrast, DF-TCM ensures that all six switches share the switching burden more evenly while still guaranteeing ZVS turn-ON, significantly improving thermal balance. Table II summarizes the comparison between different modulation methods, including the conventional continuous current mode (CCM), TCM-I, TCM-II, and DF-TCM. It is also important to distinguish between the commutation sequence and circuit topology when referring to these modulation strategies. Specifically, DF-TCM and TCM-I/II refer to the commutation sequence used in the converter, and iTCM and interleaved TCM refer to specific circuit topologies implementing TCM. These terms address two distinct aspects of a TCM-modulated converter system and should not be used interchangeably.

In practical applications as well as in the experiments conducted for this article, the proposed TCM-I, TCM-II, and DF-TCM can be implemented with the CBPWM method, where modulating signals and carrier waves are involved to generate PWM signals for the switches. In such cases, what TCM modulations differ from other conventional modulations is that the carrier waves, instead of having a fixed frequency, feature a specifically calculated time-varying frequency profile to ensure TCM currents. The modulating signals, on the other hand, are the same with conventional modulations, which means that some established strategies such as third harmonic PWM (THPWM), space vector PWM (SVPWM), or discontinuous PWM (DPWM) could easily migrate to the TCM modulations. More importantly, for multilevel converters such as the 3L-ANPC studied in this manuscript, neutral point (NP) voltage balancing has been a crucial consideration and many established active control methods for NP voltage balancing are based on the injection of certain common-mode components into the modulating signals. The carrier-based implementation of TCM makes the modulation methods compatible with these control algorithms.

TABLE II
COMPARISON OF DIFFERENT MODULATION METHODS

Modulation	Advantages	Disadvantages	Suitability
CCM	CCM places a lower computational load on the controller, improving real-time performance. It requires fewer magnetic components and supports simpler topologies, easing system design. Its harmonic spectrum is well understood, simplifying EMI filter design. Smaller current ripples also lead to lower conduction losses in switches and inductors.	CCM can result in higher switching losses due to the existing hard turn-on transitions. It also increases reverse recovery losses in the diodes, which can impact switch reliability. Additionally, the clustered harmonic spectrum demands more complex EMI filtering, often requiring larger filters.	CCM is suitable for generic application scenarios where system switching frequency is relatively low and high power density is not the main concern.
TCM-I	Same as other TCM modulations, ZVS turn-on is ensured for the whole grid period, enabling the converter to switch at a high frequency while keeping system efficiency relatively high. TCM-I features combination of HF modules and LF modules, making it possible to employ mixed switch technology, for example, Si MOSFETs for LF modules and SiC MOSFETs for HF modules.	As with other TCM schemes, the approach requires more magnetic components, increasing design complexity. It also introduces large current ripples that must be carefully managed to meet grid harmonic standards. Calculating the instantaneous switching frequency adds computational load, which can challenge the system's real-time performance. In TCM-I, modules operate at significantly different frequencies, leading to thermal imbalance among switches and complicating thermal management.	TCM is well-suited for applications demanding high power density. TCM-I, on the other hand, supports mixed switch technologies for better cost-performance trade-offs and is ideal for interleaved topologies, enabling efficient load sharing in high-power systems.
TCM-II	Same as TCM-I, a combination of HF and LF modules enables use of mixed switch technology.	Besides the disadvantages of TCM-I, TCM-II has the following drawbacks: unlike TCM-I, TCM-II requires strict synchronization between HF pairs of outer and clamping switches, posing challenges on the system reliablity; unlike TCM-I, TCM-II is not suitable to parallel interleaved circuit topology.	Generally speaking, TCM-II is unfavorable to TCM-I in most application scenarios.
DF-TCM	Higher maximum switching speed can be achieved with the same switch technology. All switches more evenly bear the residual ZVS losses, simplifying thermal analysis and design for the system.	Same as TCM-II, DF-TCM is not compatible with the interleaved circuit topology.	As compared to TCM-I, DF-TCM is suitable for application scenarios where system thermal design is of great concern. DF-TCM is suitable for iTCM circuit topology.

D. SFP Method

As discussed in Section II-B, the switching frequency must vary over time, as illustrated in Fig. 5, to achieve the desired current ripple characteristics defined by (5). In practical implementation, the instantaneous switching frequency is computed within each interrupt service routine (ISR) by the microcontroller unit (MCU). However, this approach imposes a significant computational burden on real-time applications, particularly due to the division operation in (7), which typically requires considerable processing time on most MCUs. Beyond computational challenges, the switching frequency profile in Fig. 5 contains sections with steep slopes, highlighted in red. Considering that in practice the calculation and update of f_{sw} is carried out in a regularly happening ISR in an embedded controller, these rapid increases and decreases of f_{sw} in the vicinity of 0° and 180° in fundamental period would effectively be like turning ON and OFFof a HF voltage source twice every fundamental cycle from the perspective of the *LCL* filter, which function as a resonance-exciting source for the *LCL* filter circuit, causing problems of ringing in the circuit and posing challenges to the system stability. To address these practical limitations of traditional TCM modulation, this article proposes replacing the conventional method with a SFP with offset. The SFP concept was first introduced in [16], referred to as sinusoidal-TCM (STCM), for achieving ZVS modulation in a three-phase two-level ac/dc voltage source converter (VSC). In this approach, the discontinuous f_{sw} profile of conventional TCM is replaced with a continuous function, easing both theoretical analysis and computational complexity. A more detailed theoretical analysis of STCM is provided in [27], [28], [29]. However, the switching frequency characteristics of different converter topologies vary, which affects how STCM can be applied. For examples, in a TCM-modulated three-phase two-level VSC, the local maximum switching frequency occurs at zero-crossing points, while the local minimum occurs at inductor current peaks. This property allows the STCM method in [16] to ensure ZVS throughout the fundamental period. In contrast, for topologies such as the single-phase H-bridge PFC converter or the 3L-ANPC converter studied in this article, the switching frequency dips both at the zero-crossing moment and at the current peak (cf. Fig. 5). This makes it challenging to guarantee ZVS for the full period using a simple SFP.

The SFP shown in Fig. 10 has its switching frequency curve of sinusoidal shape that centers around f_{offset} with a magnitude of f_{mag} as given by the following:

$$f_{\text{sw}}(\theta) = f_{\text{offset}} + f_{\text{mag}} \cdot \sin\left(2\theta + \frac{\pi}{2}\right). \tag{10}$$

TABLE III
COMPARISON BETWEEN THE PROPOSED SFP AND CONVENTIONAL FREQUENCY PROFILE

Frequency Profile	Features	Advantages	Disadvantages
SFP	Derived based on the conventional frequency profile. SFP employs a sinusoidal function with offset to fit the original frequency profile, which involves two additions, two multiplications and one trigonometric operation.	The method reduces computational load by minimizing mathematical operations, notably avoiding division. A freely chosen center frequency ensures a continuous profile, even when conventional methods are clamped. The smooth, sinusoidal variation in switching frequency also helps prevent unwanted resonance in the circuit.	Full ZVS is lost in the vicinity of zero crossing points. Parts of the current envelopes get expanded, leading to slight increases in RMS conduction losses.
Conventional	Derived based on accurate circuit analysis. Calculations including four multiplications, one trigonometric operation, two additions and one division.	The switching frequency is more accurate to result in the minimum required $\lvert I_{zvs}\rvert$ that ensures ZVS.	Conventional frequency profile demands greater computational resources, posing issues to real-time capability of the system. Parts of the profile curves are so steep that circuit resonance could be excited. Clamping to the limit might be necessary, which leads to discontinuity of the profile.

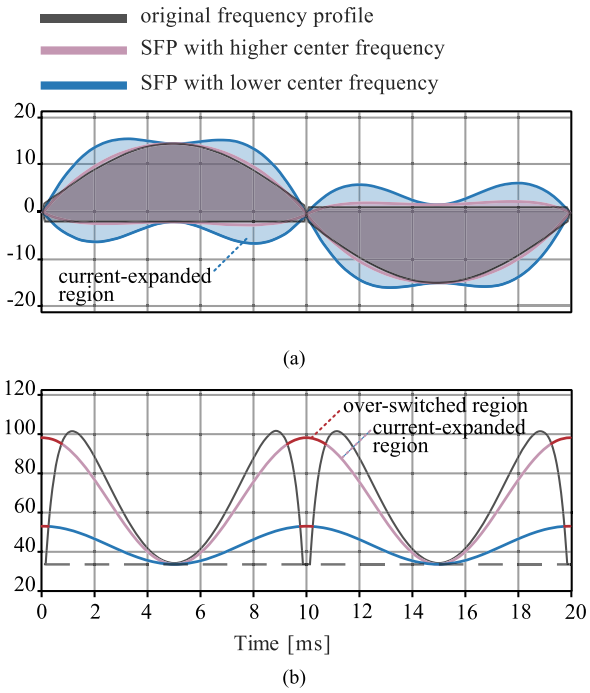

Fig. 10. Comparison of the operating waveforms for conventional frequency profile and the proposed SFP. (a) The current envelopes of the switching node current i_s. (b) The switching frequency functions with respect to time, where the line segments in red on SFP curves signify loss of full ZVS. (a) MOSFET Current i_s [A]. (b) Switching Frequency [kHz].

The center offset frequency f_{offset} serves as a degree of freedom that can be selected based on a trade-OFFbetween harmonic filtering effort and switching losses. The frequency variation magnitude f_{mag} should then be derived accordingly to ensure that the local minimum of the SFP matches $f_{sw,min}$ of the original switching frequency function in Fig. 5, i.e., $f_{offset} - f_{mag} = f_{sw,min}$. As previously mentioned, ZVS is not guaranteed throughout the entire fundamental period when using SFP. In particular, full ZVS is lost in small regions around the zero-crossing point, which are highlighted in red as over-switched regions in Fig. 10. However, it is important to note that switching losses E_{sw} are strongly correlated with the switched current I_{sw} as described by (11), where a, b, and c are component-specific curve-fitting coefficients [18].

$$E_{sw}(I_{sw}) = a + b|I_{sw}| + c|I_{sw}|^2. \tag{11}$$

Therefore, turn-ON losses are inherently minimal around the zero-crossing point, making SFP a practical and well-balanced approach for implementing TCM. This method effectively maintains ZVS for most of the operating period while only sacrificing a few switching cycles that contribute low turn-ON losses. Table III summarizes the comparison between the proposed SFP and the conventional frequency profile.

III. SYSTEM DESIGN AND ANALYSIS

A. Parameter Design Considerations

For both iTCM and interleaved TCM, the key parameter that must be determined is the range of switching frequency. On one hand, f_{sw} should have a minimum limit $f_{sw,min}$ that remains sufficiently higher than the intrinsic resonance frequency of the *LCL* filter to prevent resonant oscillation and enhance closed-loop control stability. Moreover, in iTCM additional attention is required to ensure that f_{sw} does not approach the resonant frequency of the *LC* branch circuit, as this could lead to high current circulation. This constraint implies that if f_{sw} drops below $f_{sw,min}$ at any point, it should be kept at this minimum value to prevent undesirable effects. In addition, for practical implementation, it is recommended that the preliminary choice of $f_{sw,min}$ should not be lower than 20 kHz to avoid the generation of audible noise. Within each fundamental period, f_{sw} reaches its local minimum $f_{sw,min}$ at 90°. Given an initial choice of $f_{sw,min}$, the effective inductance L in (6) can then be computed using the following:

$$L = \frac{\hat{v}_{ac}^2 \cdot (1 - M)}{4P + 2\hat{v}_{ac} \cdot |I_{zvs}|} \cdot \frac{1}{f_{sw,min}}. \tag{12}$$

On the other hand, for practical implementation, f_{sw} cannot be excessively high, necessitating the definition of an upper limit f_{max} before parameter design. By taking the first derivative of

(7) and solving for zeros, the angle $\theta_{\max}$ at which $f_{\rm sw}$ reaches its local maximum, can be determined, as given in (13) show at the bottom of this page. Consequently, $f_{\rm sw,max}$ and the switching frequency ratio γ, defined as the ratio of $f_{\rm sw,max}$ to $f_{\rm sw,min}$, can be derived as shown in (14) show at the bottom of this page. In this article, $f_{\max}$ is set to 150 kHz for both simulation and hardware experiment. Whenever $f_{\rm sw}$ attempts to exceed $f_{\max}$, it is clamped at this limit. As a result, the current envelopes of $i_{\rm s}$ expand, leading to increased conduction losses. Therefore, it is preferable to keep $f_{\rm sw,max}$ below $f_{\max}$ to prevent clamping and ensure that the switching frequency remains a continuous time function.

Another critical consideration for the studied converter system is the resonance frequency $f_{\rm res}$ of the LCL filter, as it plays a crucial role in avoiding undesired circuit resonance and maintaining control stability. For a TCM-modulated 3L-ANPC converter, as depicted in Fig. 3, $f_{\rm res}$ is given by the following:

$$f_{\rm res} = \frac{1}{2\pi} \cdot \sqrt{\frac{L_{\rm c} + L_{\rm g}}{L_{\rm c} L_{\rm g} C_{\rm f}}}. \tag{15}$$

At the preliminary design stage, $f_{\rm sw,min}$ should be chosen well away from $f_{\rm res}$ to prevent instability and unwanted resonance effects. For an iTCM-modulated topology, as shown in Fig. 6(b), additional caution is required regarding the resonance frequency $f_{\rm res,LC}$ of the LC branch circuit, which is connected in series. This frequency can be determined using (16). If $f_{\rm sw}$ approaches $f_{\rm res,LC}$, it can lead to excessive short-circuit currents, potentially damaging components and compromising system reliability

$$f_{\rm res,LC} = \frac{1}{2\pi} \cdot \sqrt{\frac{1}{L_{\rm b} C_{\rm b}}}. \tag{16}$$

For the interleaved topology shown in Fig. 6(a), the effective resonance frequency $f_{\rm res}$, which accounts for all the parallel-connected switching cells along with $L_{\rm g}$ and $C_{\rm f}$, is lower than the resonance frequency given in (15). Assume there are N switching cells, each with the same inductance value $L_{\rm c}$. The voltage at the switching node of each cell can be modeled as a harmonic voltage source with phase shift of $(2n\pi/N)$, where n denotes the nth switching cell, ranging from 0 to $(N-1)$. To determine the effective resonance frequency, the circuit is analyzed by finding its Thevenin equivalent from the dc side to the common connection point of all output terminals of $L_{\rm c}$. The Thevenin-equivalent impedance, denoted as $L_{\rm Th}$, is given by $L_{\rm c}/N$. This value represents the effective system inductance used in the calculation of $f_{\rm res}$. In addition, the Thevenin-equivalent voltage source $V_{\rm Th}$ exhibits harmonic spectra starting from N times the fundamental frequency of a single switching cell. Consequently, the effective resonance frequency of the interleaved system, denoted as $f_{\rm res,int}$, can be derived as (17). This formulation highlights how parallel interleaving reduces the effective system inductance and shifts the resonance frequency, impacting the overall system stability and harmonic behavior. As illustrated in Fig. 11, $f_{\rm res,int}$ decreases as the number of parallel switching cells increases, emphasizing the importance of choosing $f_{\rm sw,min}$ at a safe margin away from $f_{\rm res,int}$ to prevent unwanted circuit oscillations and ensure stable operation

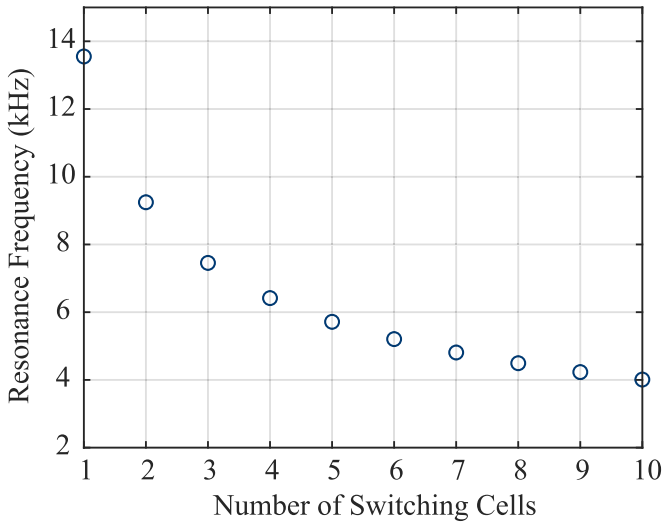

Fig. 11. Typical characteristic curve of $f_{\rm res,int}$ with respect to the number of parallel switching cells N.

$$f_{\rm res,int} = \frac{1}{2\pi} \cdot \frac{1}{N} \cdot \sqrt{\frac{L_{\rm c} + N \cdot L_{\rm g}}{L_{\rm c} L_{\rm g} C_{\rm f}}}. \tag{17}$$

B. Conduction Loss Modeling

A theoretical model for semiconductor losses $P_{\rm semi}$ is crucial for the thermal analysis and design of the studied iTCM 3L-ANPC system. Generally, $P_{\rm semi}$ can generally be grouped into two categories: conduction losses ($P_{\rm cond}$), incurred when the device is conducting current; and switching losses ($P_{\rm sw}$), generated during circuit transitions. Thus, the total semiconductor losses can be expressed as $P_{\rm semi} = P_{\rm cond} + P_{\rm sw}$. For unipolar semiconductors, $P_{\rm cond}$ is determined by the RMS current flowing through the semiconductor device of interest, denoted as $I_{\rm sw,rms}$, and

$$\theta_{\max} = \arcsin\left(\frac{1}{2MP} \cdot \left(\sqrt{M^2 \cdot \hat{v}_{\rm ac}^2 \cdot |I_{\rm zvs}|^2 + 2M \cdot P \cdot \hat{v}_{\rm ac} \cdot |I_{\rm zvs}|} - M \cdot \hat{v}_{\rm ac} \cdot |I_{\rm zvs}|\right)\right) \tag{13}$$

$$\begin{cases} f_{\rm sw,max} = \dfrac{P \cdot \sqrt{\beta \cdot (2P+\beta)} - \beta^2 + \beta \cdot \sqrt{\beta \cdot (2P+\beta)} - 2P \cdot \beta}{4P^2 \cdot \sqrt{\beta \cdot (2P+\beta)}} \cdot \dfrac{1}{L} \\ \gamma = \dfrac{f_{\rm sw,max}}{f_{\rm sw,min}} = \dfrac{(4P + 2|I_{\rm zvs}| \cdot \hat{v}_{\rm ac}) \cdot \left(\beta^2 - P \cdot \sqrt{\beta \cdot (2P+\beta)} + 2P \cdot \beta - \beta \cdot \sqrt{\beta \cdot (2P+\beta)}\right)}{4P^2 \cdot (M-1) \cdot \sqrt{\beta \cdot (2P+\beta)}} \\ \beta = M \cdot \hat{v}_{\rm ac} \cdot |I_{\rm zvs}| \end{cases} . \tag{14}$$

the ON-state resistance $R_{\mathrm{ds,on}}$. For a triangular-shaped current waveform bounded by upper and lower envelopes i_{env}^{+} and i_{env}^{-}, the RMS current i_{rms} over one ripple interval can be calculated using the following:

$$i_{\mathrm{rms}}^2 = \frac{1}{3}\left(i_{\mathrm{env}}^{+\,2} + i_{\mathrm{env}}^{+} \cdot i_{\mathrm{env}}^{-} + i_{\mathrm{env}}^{-\,2}\right). \tag{18}$$

Accordingly, the RMS value of i_{s} over one fundamental period, denoted as $I_{\mathrm{s,rms}}$ can be calculated by the following:

$$\begin{aligned} I_{\mathrm{s,rms}}^2 &= \frac{1}{\pi}\int_0^{\pi} i_{\mathrm{s}}^2(\theta)\,\mathrm{d}\theta \\ &= \frac{1}{\pi}\int_0^{\pi} \frac{1}{3}\Big((I_{\mathrm{zvs}} + 2\cdot\hat{i}_{\mathrm{ac}}\cdot\sin\theta)^2 \\ &\quad + (I_{\mathrm{zvs}} + 2\cdot\hat{i}_{\mathrm{ac}}\cdot\sin\theta)\cdot(-I_{\mathrm{zvs}}) + (-I_{\mathrm{zvs}})^2\Big)\,\mathrm{d}\theta \\ &= \frac{2}{3}\hat{i}_{\mathrm{ac}}^2 + \frac{4}{3\pi}\hat{i}_{\mathrm{ac}}\,I_{\mathrm{zvs}} + \frac{1}{3}I_{\mathrm{zvs}}^2. \end{aligned} \tag{19}$$

By circuit symmetry, the two inner switches S_2 and S_3 are stressed with the same $I_{\mathrm{s,rms}}$, and therefore, the corresponding RMS current $I_{\mathrm{in,rms}}$ is given by the following:

$$I_{\mathrm{in,rms}}^2 = \frac{1}{3}\hat{i}_{\mathrm{ac}}^2 + \frac{2}{3\pi}\hat{i}_{\mathrm{ac}}\cdot\ I_{\mathrm{zvs}} + \frac{1}{6}I_{\mathrm{zvs}}^2. \tag{20}$$

An examination on (6) reveal that the conduction time allocations for the two outer switches (S_1, S_4) and the two clamping switches (S_5, S_6) are not equal. For the outer switches, the RMS current $I_{\mathrm{out,rms}}$ can be determined by multiplying the integrand by the corresponding time allocation percentage, as expressed in (21). The $\frac{1}{2}$ factor in the equation accounts for the fact that each outer switch conducts only for half of the fundamental period.

$$\begin{aligned} I_{\mathrm{out,rms}}^2 &= \frac{1}{2}\cdot\frac{1}{\pi}\int_0^{\pi}\frac{1}{3}\cdot\frac{\hat{v}_{\mathrm{ac}}\cdot\sin\theta}{V_{\mathrm{dc}}/2}\Big((I_{\mathrm{zvs}} + 2\hat{i}_{\mathrm{ac}}\cdot\sin\theta)^2 \\ &\quad + (I_{\mathrm{zvs}} + 2\hat{i}_{\mathrm{ac}}\cdot\sin\theta)\cdot(-I_{\mathrm{zvs}}) + (-I_{\mathrm{zvs}})^2\Big)\,\mathrm{d}\theta \\ &= \frac{\hat{v}_{\mathrm{ac}}}{3\pi V_{\mathrm{dc}}}\cdot\int_0^{\pi}\Big(4\hat{i}_{\mathrm{ac}}\cdot\sin^3\theta + 2I_{\mathrm{zvs}}\cdot\hat{i}_{\mathrm{ac}}\cdot\sin^2\theta \\ &\quad + I_{\mathrm{zvs}}^2\cdot\sin\theta\Big)\,\mathrm{d}\theta \\ &= \frac{\hat{v}_{\mathrm{ac}}}{3\pi V_{\mathrm{dc}}}\cdot\left(\frac{16}{3}\hat{i}_{\mathrm{ac}}^2 + \pi\cdot I_{\mathrm{zvs}}\cdot\hat{i}_{\mathrm{ac}} + 2I_{\mathrm{zvs}}^2\right). \end{aligned} \tag{21}$$

Since the clamping switches and the outer switches together share the currents through the inner switches, the RMS current for the clamping switches $I_{\mathrm{clp,rms}}$ can be obtained by taking the subtraction as given in the following:

$$I_{\mathrm{clp,rms}}^2 = I_{\mathrm{in,rms}}^2 - I_{\mathrm{out,rms}}^2. \tag{22}$$

Note that the above derivation of the RMS current for all the six switches is valid for TCM-I, TCM-II, and DF-TCM.

IV. Experimental Verification

Fig. 12 shows the hardware prototype used to verify the feasibility of the proposed modulation methods on the studied converter system. In the experiments, the 3L-ANPC converter works in inverter mode with the nominal system specifications and key parameters listed in Tables IV and V, respectively. The waveforms are recorded with the KEYSIGHT InfiniiVision DSOX3024 A oscilloscope, and the conversion efficiency is measured with a YOKOGAWA WT5000 power analyzer. The AMD Zynq 7010 SoC is employed as MCU platform for the experiments, which provides both accuracy and flexibility in control.

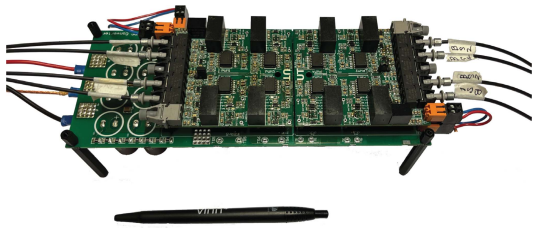

Fig. 12. Hardware prototype of the 3L-ANPC converter power circuit used in the experiments.

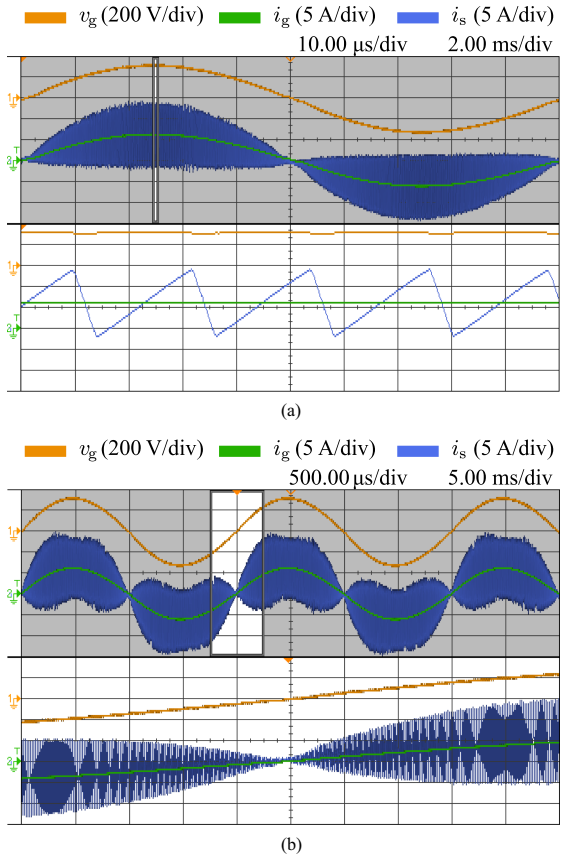

Fig. 13. Recorded waveforms of the proposed soft-switched 3L-ANPC converter employing DF-TCM. (a) Center offset frequency f_{offset} at 44.6 kHz and frequency variation magnitude f_{mag} at 22.6 kHz. (b) Center offset frequency f_{offset} at 30 kHz and frequency variation magnitude f_{mag} at 8 kHz.

As discussed in Section II-D, SFP provides a practical implementation of TCM for the 3L-ANPC topology by mitigating unwanted circuit resonance. Therefore, SFP is employed in all the experiments conducted in this section.

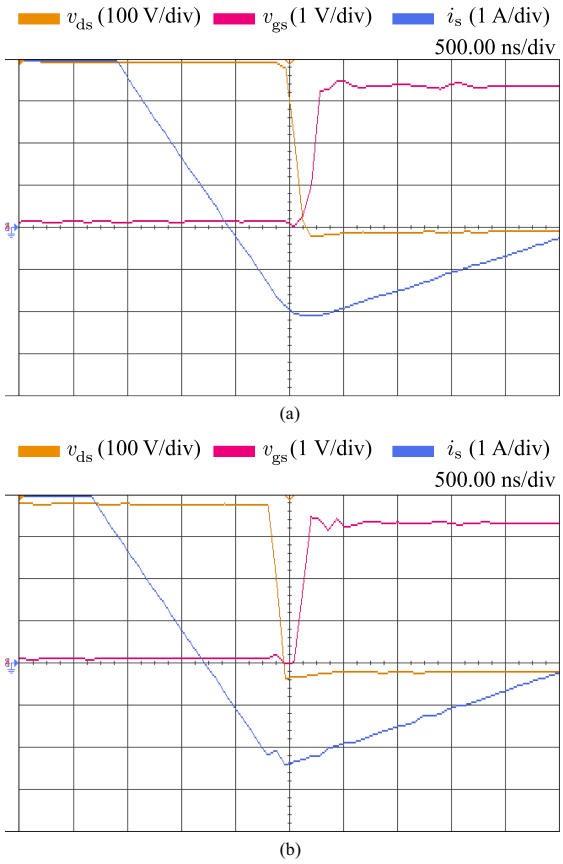

Fig. 14. Zoomed-in waveforms of the gate signal v_{gs}, the drain-to-source voltage v_{ds}, the semiconductor current i_s during the turn-ON process of: (a) Outer switch S_1; (b) Inner switch S_2.

TABLE IV
SYSTEM SPECIFICATIONS FOR HARDWARE EXPERIMENTS

System Specifications	Symbol	Value
AC Phase Voltage	v_{ac}	230 V RMS
Grid Frequency	f_0	50 Hz
DC Voltage	V_{dc}	800 V
Modulation Index	M	0.8132
Nominal Output Power	P_o	1.058 kW
Reverse Current Reference	$\|I_{zvs}\|$	1.5 A

Fig. 13(a) presents the recorded ac output voltage and key current waveforms under nominal operating conditions, using the circuit in Fig. 3 to validate the DF-TCM modulation. In Fig. 13(a), the phase-to-mid-point output voltage have a sinusoidal shape. It can be seen that i_s has a triangular shape and reverses its polarity within each switching cycle. Since the center offset frequency f_{offset} for Fig. 13(a) is relatively high at 44.6 kHz, the current expansion is not obvious. Fig. 13(b) shows the case where the same operating condition as for Fig. 13(a) is applied but f_{offset} is lower at 30 kHz. It can be observed that the extent of current expansion is much higher for the case with f_{offset} at 30 kHz as compared to that with f_{offset} at 44.6 kHz. Fig. 14 shows the zoomed-in waveforms of soft-switched TCM at the turn-ON moment of the current commutation. It is verified

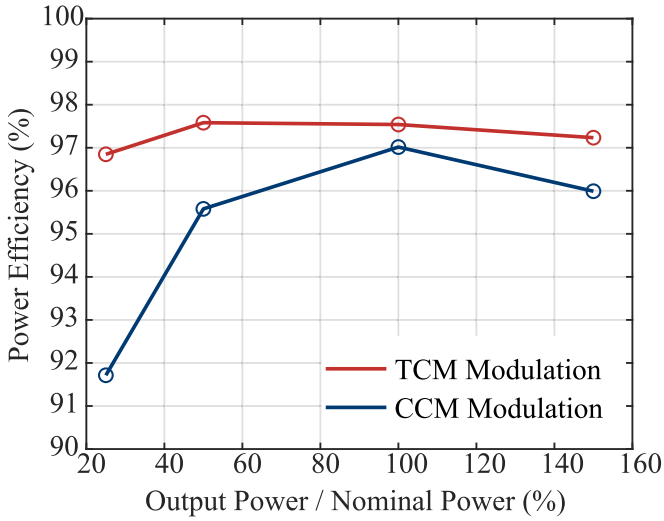

Fig. 15. Measured power conversion efficiency curves for the TCM and the CCM modulated 3L-ANPC converter.

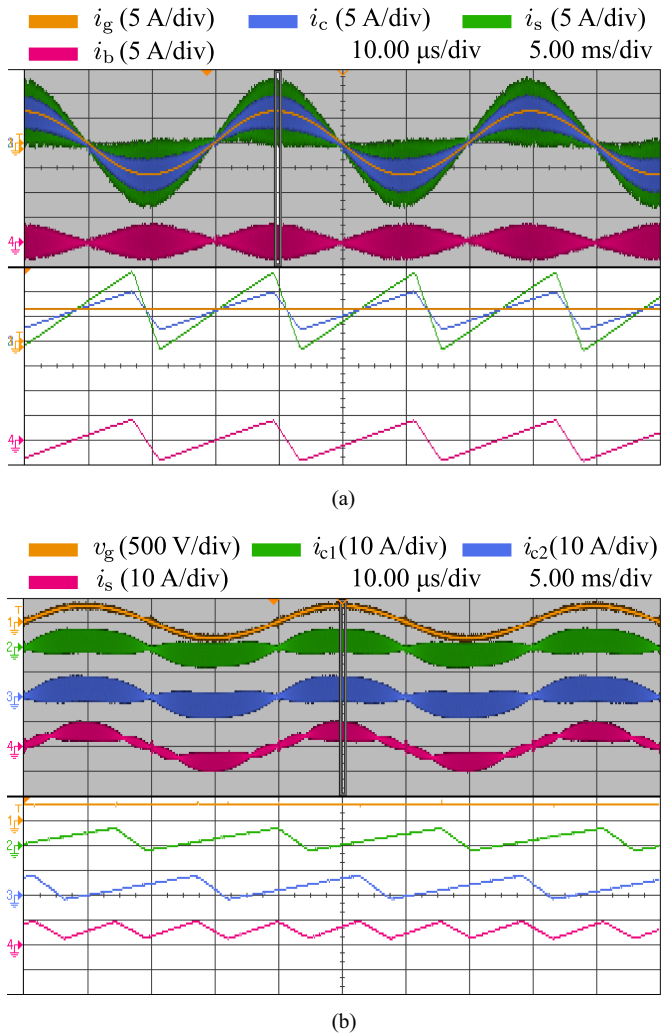

Fig. 16. Recorded waveforms of the proposed soft-switched 3L-ANPC converter employing TCM-I. (a) iTCM circuit topology with center offset frequency f_{offset} at 90 kHz and frequency variation magnitude f_{mag} at 45 kHz. (b) Interleaved-TCM circuit topology with center offset frequency f_{offset} at 67 kHz and frequency variation magnitude f_{mag} at 28 kHz.

TABLE V
KEY CIRCUIT PARAMETERS FOR HARDWARE EXPERIMENTS

Basic TCM		
Grid-Side Inductance	L_g	500 μH
Converter-Side Inductance	L_c	80 μH
LCL Filter Capacitance	C_f	2.2 μF
iTCM		
Grid-Side Inductance	L_g	300 μH
Converter-Side Inductance	L_c	160 μH
LC Branch Inductance	L_b	160 μH
LCL Filter Capacitance	C_f	1.1 μF
LC Branch Capacitance	C_b	1.1 μF
Current Sharing Coefficient	r	0.5
interleaved TCM		
Grid-Side Inductance	L_g	300 μH
Converter-Side Inductance	$L_{c1/2}$	160 μH
Number of Cells	N	2
LCL Filter Capacitance	C_f	2.2 μF

that by reversing the current polarity of i_s the blocked voltage is able to fall from $V_{dc}/2$ to zero before the gate signal is applied.

Fig. 15 compares the measured power conversion efficiency for the TCM and the traditional CCM modulations at different output powers as percentages of the nominal power at 1.058 kW. The measured converter efficiency at the nominal output is 97.54% for the TCM modulated system (f_{offset} at 44.6 kHz and f_{mag} at 22.6 kHz), as compared to 97.01% for the CCM modulated one with a fixed switching frequency at 44.6 kHz, proving the effectiveness of soft switching. Note that in the experiments the ac side current peaks at 6.5 A under nominal load and $|I_{zvs}|$ of 1.5 A is comparable to this value. The ratio of $|I_{zvs}|$ to $\hat{i}_{ac}$ is much larger than that for practical applications, where $|I_{zvs}|$ is usually only up to 5% of $\hat{i}_{ac}$. As in (5), the presence of $|I_{zvs}|$ enlarges the current ripples and leads to extra conduction losses. Based on (19), the less the ratio of $|I_{zvs}|$ to $\hat{i}_{ac}$, the less influence a fixed $|I_{zvs}|$ has on the RMS current, and consequently, TCM modulation would have a larger improvement on the system efficiency as compared to CCM modulation.

Fig. 16 shows the experimental results of the iTCM modulation and interleaved-TCM modulation respectively, where for both cases TCM-I method is employed. In Fig. 16(a), approximately half of the current ripples in i_s are shared by i_b in the notch filter as L_c and L_b are designed to have the same value. Note that to keep the same apparent switching frequency in current ripples as that in the basic TCM scheme, the carrier frequency used in TCM-I needs to be double of that for the DF-TCM. For the waveforms of the interleaved-TCM modulation in Fig. 16(b), the effective current harmonics in i_s are greatly decreased due to the fact that i_{c1} and i_{c2} are equally sharing the load current and are exactly 180° out of phase. One of the advantages of the interleaved-TCM is the flexibility to add more parallel-connected switching cells in case of an increase in load or a desire to further decrease the harmonic contents in i_s.

V. CONCLUSION

This work presents a comprehensive analysis of expanding the soft-switching TCM modulation technique to the 3L-ANPC converter, addressing key implementation challenges. First, two fundamental commutation sequences, TCM-I and TCM-II, are introduced, followed by the derivation of a more advantageous DF-TCM scheme. In addition, to replace the computationally intensive and resonance-prone switching frequency profile, this article proposes SFP as a practical alternative. The study further examines the impact of various circuit parameters and design considerations, along with developing a conduction loss model for accurate system evaluation. Finally, a hardware prototype is constructed to validate the proposed TCM strategy, demonstrating a measured system efficiency of 97.54% with output power at 1.058 kW, thereby confirming the effectiveness of the approach.

REFERENCES

[1] A. Poorfakhraei, M. Narimani, and A. Emadi, "A review of multilevel inverter topologies in electric vehicles: Current status and future trends," *IEEE Open J. Power Electron.*, vol. 2, pp. 155–170, 2021.

[2] G. Guo et al., "Series-connected-based offshore wind farms with full-bridge modular multilevel converter as grid- and generator-side converters," *IEEE Trans. Ind. Electron.*, vol. 67, no. 4, pp. 2798–2809, Apr. 2020.

[3] H. Cheng, Z. Zhao, C. Wang, W. Yuan, and J. Hao, "A novel DC-link capacitor voltage balance control based on coordination of rectifier–inverter stage in a modified unidirectional five-level converter for AC motor drives," *IEEE Trans. Emerg. Sel. Topics Power Electron.*, vol. 11, no. 5, pp. 5156–5168, Oct. 2023.

[4] T. B. Soeiro, K.-B. Park, and F. Canales, "High voltage photovoltaic system implementing Si/SiC-based active neutral-point-clamped converter," in *Proc. 43rd Annu. Conf. IEEE Ind. Electron. Soc.*, 2017, pp. 1220–1225.

[5] J. Rodriguez, J.-S. Lai, and F. Z. Peng, "Multilevel inverters: A survey of topologies, controls, and applications," *IEEE Trans. Ind. Electron.*, vol. 49, no. 4, pp. 724–738, Aug. 2002.

[6] R. H. Baker, "Bridge converter circuit," in US Patent US4270163, 1979.

[7] A. Nabae, I. Takahashi, and H. Akagi, "A new neutral-point-clamped PWM inverter," *IEEE Trans. Ind. Appl.*, vol. IA-17, no. 5, pp. 518–523, 1981.

[8] B. Bijlenga, "A converter device," US Patent EP1051799B1, 1998.

[9] T. Bruckner, S. Bernet, and H. Guldner, "The active NPC converter and its loss-balancing control," *IEEE Trans. Ind. Electron.*, vol. 52, no. 3, pp. 855–868, Jun. 2005.

[10] T. Bruckner, S. Bernet, and P. K. Steimer, "Feedforward loss control of three-level active NPC converters," *IEEE Trans. Ind. Appl.*, vol. 43, no. 6, pp. 1588–1596, Nov./Dec. 2007.

[11] Y. Deng, J. Li, K. H. Shin, T. Viitanen, M. Saeedifard, and R. G. Harley, "Improved modulation scheme for loss balancing of three-level active NPC converters," *IEEE Trans. Power Electron.*, vol. 32, no. 4, pp. 2521–2532, Apr. 2017.

[12] C. Marxgut, J. Biela, and J. W. Kolar, "Interleaved triangular current mode (TCM) resonant transition, single phase PFC rectifier with high efficiency and high power density," in *Proc. IEEE Int. Power Electron. Conf.*, Jun. 2010, pp. 1725–1732.

[13] U. Badstuebner, J. Miniboeck, and J. W. Kolar, "Experimental verification of the efficiency/power-density (η-ρ) pareto front of single-phase double-boost and TCM PFC rectifier systems," in *Proc. 28th Annu. IEEE Appl. Power Electron. Conf. Expo.*, Mar. 2013, pp. 1050–1057.

[14] G. Zhang, Y. Wu, J. Xu, and T. B. Soeiro, "iTCM-operated three-phase three-wire voltage-source converter system featuring capacitor-split virtual ground connection," *IEEE Trans. Power Electron.*, vol. 39, no. 8, pp. 9415–9429, 2024.

[15] D. Rothmund, T. Guillod, D. Bortis, and J. W. Kolar, "99.1% efficient 10 kV SiC-based medium-voltage ZVS bidirectional single-phase PFC AC/DC stage," *IEEE J. Emerg. Sel. Topics Power Electron.*, vol. 7, no. 2, pp. 779–797, Jun. 2019.

[16] M. Haider et al., "Novel ZVS S-TCM modulation of three-phase AC/DC converters," *IEEE Open J. Power Electron.*, vol. 1, pp. 529–543, 2020.

[17] G. Yu, J. Dong, T. B. Soeiro, G. Zhu, Y. Yao, and P. Bauer, "Three-mode variable-frequency ZVS modulation for four-switch buck boost converters with ultra-high efficiency," *IEEE Trans. Power Electron.*, vol. 38, no. 4, pp. 4805–4819, Apr. 2023.

[18] J. Xu, T. B. Soeiro, Y. Wang, F. Gao, H. Tang, and P. Bauer, "A hybrid modulation featuring two-phase clamped discontinuous PWM and zero voltage switching for 99% efficient DC-type EV charger," *IEEE Trans. Veh. Technol.*, vol. 71, no. 2, pp. 1454–1465, Feb. Feb. 2022.
[19] T. Liu, C. Chen, K. Xu, Y. Zhang, and Y. Kang, "GaN-based megahertz single-phase inverter with a hybrid TCM control method for high efficiency and high-power density," *IEEE Trans. Power Electron.*, vol. 36, no. 6, pp. 6797–6813, Jun. 2021.
[20] S. Miric, P. S. Niklaus, J. Huber, C. Stäger, M. Haider, and J. W. Kolar, "Analysis and experimental verification of the EMI signature of three-phase three-level TCM soft-switching converter systems," *IEEE Access*, vol. 11, pp. 57391–57400, 2023.
[21] J. Sun, Y. Wu, T. B. Soeiro, Z. Qin, and P. Bauer, "ZVS turn-on integrated triangular current mode three-phase PFC for EV on-board chargers," in *Proc. IEEE 20th Int. Power Electron. Motion Control Conf.*, 2022, pp. 285–294.
[22] C. Marxgut, F. Krismer, D. Bortis, and J. W. Kolar, "Ultraflat interleaved triangular current mode (TCM) single-phase PFC rectifier," *IEEE Trans. Power Electron.*, vol. 29, no. 2, pp. 873–882, Feb. 2014.
[23] M. Kasper, R. M. Burkart, G. Deboy, and J. W. Kolar, "ZVS of power MOSFETs revisited," *IEEE Trans. Power Electron.*, vol. 31, no. 12, pp. 8063–8067, Dec. 2016.
[24] D. Floricau, E. Floricau, and M. Dumitrescu, "Natural doubling of the apparent switching frequency using three-level ANPC converter," in *Proc. Int. Sch. Nonsinusoidal Curr. Compensation*, 2008, pp. 1–6.
[25] D. Rothmund, D. Bortis, and J. W. Kolar, "Accurate transient calorimetric measurement of soft-switching losses of 10-kV SiC MOSFETs and diodes," *IEEE Trans. Power Electron.*, vol. 33, no. 6, pp. 5240–5250, Jun. 2018.
[26] M. Haider et al., "Analytical calculation of the residual ZVS losses of TCM-operated single-phase PFC rectifiers," *IEEE Open J. Power Electron.*, vol. 2, pp. 250–264, 2021.
[27] Y. Wu, J. Xu, T. B. Soeiro, M. Stecca, and P. Bauer, "Optimal periodic variable switching PWM for harmonic performance enhancement in grid-connected voltage source converters," *IEEE Trans. Power Electron.*, vol. 37, no. 6, pp. 7247–7262, Jun. 2022.
[28] Y. Wu, Z. Qin, T. B. Soeiro, and P. Bauer, "Interleaved AC/DC converter operating with ZVS sinusoidal triangular-current-mode (S-TCM) for reduced voltage harmonics generation," in *Proc. IEEE Energy Convers. Congr. Expo.*, 2023, pp. 161–167.
[29] Y. Wu, J. Xu, T. B. Soeiro, P. Bauer, and Z. Qin, "Frequency design of three-phase active front-end converter with reduced filter in EV chargers," *IEEE Trans. Transp. Electrific.*, vol. 10, no. 4, pp. 10083–10101, Dec. 2024.

Gang Zhang (Student Member, IEEE) was born in Taiyuan, China, in 1995. He received the B.S. degree in electrical engineering from the Hong Kong Polytechnic University, Hong Kong, in 2018, and the M.Sc. degree in information technology and electrical engineering from the Swiss Federal Institute of Technology (ETH), Zurich, Switzerland, in 2023. Since 2023, he has been working toward the Ph.D. degree in electrical engineering with Power Electronics Group (PE), University of Twente, Enschede, The Netherlands.

His research interests include topology and modulation of power converters.

Yang Wu (Student Member, IEEE) received the B.S. degree in electrical engineering and eutomation from Southeast University, Nanjing, China, in 2017, and the M.Sc. (*cum laude*) and Ph.D. degrees in electrical power engineering from Delft University of Technology, Delft, The Netherlands, in 2019 and 2024, respectively.

From January to April in 2024, he was a Visiting Scholar with Princeton Power Electronics Research Lab, Princeton University, Princeton, NJ, USA. Since August 2024, he has been a Research Scientist with ABB Corporate Research Center, Sweden. His current research interests include the modeling, control and variable switching frequency modulation of the power converter for grid-applications.

Rui Qiang (Student Member, IEEE) received the B.S. degree in electrical engineering and automation from Northwestern Polytechnical University, Xi'an, China, in 2020, and the M.Sc. degree in electrical power engineering from the Delft University of Technology, Delft, the Netherlands, in 2022. Since 2023, he has been working toward the Ph.D. degree in electrical engineering with the Power Electronics Group (PE), University of Twente, Enschede, The Netherlands.

His research interests include intelligent gate drivers, power loss measurement, and modeling of wide-bandgap semiconductor devices in power electronic systems.

Prasanth Venugopal (Senior Member, IEEE) received the M.Sc. degree (*cum laude*) in electrical power engineering and the Ph.D. degree in magnetic energy transfer in roads, both from Delft University of Technology, The Netherlands, in 2012 and 2016, respectively.

He worked as a Senior Electrical Engineer with Qualcomm Halo and later as a Technical Specialist with TDK Europe GmbH, focusing on wireless EV charging, high-frequency magnetics, and power electronics for xEV platforms. Since 2020, he has been an Assistant Professor with the Power Electronics Group, University of Twente. His research interests cover applications of power magnetics and passive devices, intelligent electronics to battery management systems (EIS based intelligent prognostics and applications of AI), energy storage management and wireless power transfer. His designs target applications such as grid-connected systems, EV charging systems, and modular battery packs. He is mission leader of the UT Battery Centre and an active contributor to the Hydrogen UT (Hy.UT) initiative. He has led or co-led major projects including EU Horizon, EU Widera and multiple NWO Projects.

Dr. Venugopal was an Associate Editor for IEEE TRANSACTIONS ON TRANSPORTATION ELECTRIFICATION and contributes actively to IEEE PELS, IAS, and IES. His recognitions include the IEEE PEMC Best Poster Prize, multiple society prizes including IAS Ph.D. Thesis Award.

Junzhong Xu (Member, IEEE), photograph and biography not available at the time of publication.

Thiago Batista Soeiro (Senior Member, IEEE) received the B.S. (Hons.) and M.S. degrees from the Federal University of Santa Catarina, Florianopolis, Brazil, in 2004 and 2007, respectively, and the Ph.D. degree from the Swiss Federal Institute of Technology, Zurich, Switzerland, in 2012, all in electrical engineering.

He was a Visiting Scholar with the Power Electronics and Energy Research Group, Concordia University, Montreal, QC, Canada, and with the Center for Power Electronics Systems, Blacksburg, VA, USA, respectively. From 2012 to 2013, he was a Researcher with the Power Electronics Institute, Federal University of Santa Catarina. From 2013 to 2018, he was a Senior Scientist with the Corporate Research Center, ABB Switzerland Ltd., Baden-Dattwil, Switzerland. From 2018 to 2022, he was an Associate Professor with the dc Systems, Energy Conversion and Storage Group, Delft University of Technology, Delft, The Netherlands. From January to October 2022, he was with the Power Management and Distribution Section (TEC-EPM) for the European Space Research and Technology Centre, Noordwijk, The Netherlands. Since October 2022, he has been a Full Professor in power electronics with the Power Electronics Group, University of Twente, Enschede, The Netherlands. His research interests include advanced high-power converters and dc system integration.

Dr. Soeiro is a recipient of the 2013 IEEE Industrial Electronics Society Best Conference Paper Award and the Best Paper Awards in the following IEEE conferences: International Conference on Power Electronics (ECCE Asia 2011), the International Conference on Industrial Technology (ICIT 2013), the Conference on Power Electronics and Applications EPE'15 (ECCE Europe 2015), and the International Conference on Power Electronics and Motion Control 2020 and 2022 (PEMC 2020 and 2022).